Supplemental Material for "Cell Motility Dependence on Adhesive Wetting"

PHASE FIELD MODEL OF CELL MOTILITY

The equations for the phase-field cross section model are:

$$\frac{\partial\phi(\boldsymbol{r},t)}{\partial t} = -\boldsymbol{u}\cdot\nabla\phi(\boldsymbol{r},t) + \Gamma(\epsilon\nabla^2\phi - G'/\epsilon + c\epsilon|\nabla\phi|) \tag{S1}$$

$$\nabla\cdot[\nu\phi(\nabla\boldsymbol{u}+\nabla\boldsymbol{u}^T)] + \boldsymbol{F}_{sub} + \boldsymbol{F}_{mem} + \boldsymbol{F}_{area} + \nabla\cdot\sigma^a = 0. \tag{S2}$$

Here, ϕ describes the field of the cell. The double-well potential is defined as $G = 18\phi^2(1-\phi)^2$ and the curvature is computed as $c = -\nabla\cdot(\nabla\phi/|\nabla\phi|)$ while Γ is a relaxation coefficient. The force terms are explicitly explained below.

The substrate force contains the cell-substrate adhesion and friction: $\boldsymbol{F}_{sub} = \boldsymbol{F}_{adh} + \boldsymbol{F}_{fric}$, where

$$\boldsymbol{F}_{fric} = -\xi_s\chi\boldsymbol{u} - \xi_d\boldsymbol{u},\ \boldsymbol{F}_{adh} = \frac{\delta H(\phi,\chi)}{\delta\phi}\nabla\phi.$$

Here, $\boldsymbol{u}$ is the velocity field of the actin fluid and ξ_s, ξ_d are the cell-substrate friction coefficient and damping coefficient, respectively. χ is the field describing the substrate, and $H(\phi,\chi)$ is the interaction potential between the cell and substrate. The The cell moves either on top of a plain substrate or between a top and bottom substrate. The location of these substrates is given by a field $\chi(y)$ with a boundary width of δ (Fig. S1). Here, $\chi = 1$ indicates the substrate into which the cell cannot penetrate, and $\chi = 0$ indicates the region accessible to the cell. In our simulations, the substrate is parallel to the x direction and, for the case of a single substrate located at $y = y_B$, χ is written as

$$\chi(y) = \frac{1}{2} - \frac{1}{2}\tanh\{3(y-y_B)/\delta\},$$

For a chamber with a parallel top substrate located at $y = y_T$ this becomes

$$\chi(y) = \frac{1}{2} + \frac{1}{2}\tanh\{3[|y-(y_T+y_B)/2| - (y_T-y_B)/2]/\delta\}.$$

Given ϕ and χ, the interaction potential is:

$$H(\phi,\chi) = \int d\boldsymbol{r}^2\phi^2(\phi-2)^2W(\chi),$$

where $W(\chi)$ contains an attractive term, corresponding to adhesion, and a repulsive term, corresponding to the non-penetrability of the substrate. For the bottom substrate, we use

$$W(\chi) = -2A\frac{G(\chi)}{\delta} + \frac{g}{2}\chi(y+\epsilon), \tag{S3}$$

while the potential for the top substrate has an identical form with ϵ replaced by $-\epsilon$. Here, A is the adhesion energy per unit length, g is a parameter that measures the penalty of overlap between cell and substrate [1], and G is a double-well potential $G(\chi) = 18\chi^2(1-\chi)^2$. The energy function

$$H(\phi,\chi) = \int \phi^2(\phi-2)^2W(\chi)d^2\boldsymbol{r}$$

corresponds, in the sharp interface limit, to an adhesive energy equal to $-Al$ where l is the length of the cell in contact with the substrate. Note that the inclusion of the $\phi^2(\phi-2)^2$ results in a force that only vanishes outside the membrane [2]. In our simulations we take $\delta = \epsilon/2$. For this choice of δ we simulated cells without any propulsive force. The resulting static shapes can be directly compared to standard energy minimization simulations. Fig. S3 shows that the phase field shapes agree well with shapes obtained using Surface Evolver, a simulation tool that evolves surfaces toward minimal energy by a gradient descent method [3].

The contribution from both the tension and bending of the membrane is captured by $\boldsymbol{F}_{mem}$. In our simulation we ignore the bending term since it contributes little to the shape of cell. The tension energy is given by [4, 5]:

$$H_{ten} = \int\frac{\gamma}{2}[\epsilon|\nabla\phi|^2 + \frac{G(\phi)}{\epsilon}]d^2\boldsymbol{r},$$

resulting in $\boldsymbol{F}_{mem} = \frac{\delta H_{ten}}{\delta \phi}\nabla\phi$. Area conservation is introduced via $\boldsymbol{F}_{area} = M_a(\int \phi d\boldsymbol{r}^2 - A_0)\nabla\phi$ with A_0 the prescribed area size, and M_a a parameter which controls the strength of the area constraint [4].

The active stress term in our model, $\sigma^a = -\eta_a G(\psi)\phi\rho_a\epsilon|\nabla\phi|^2\hat{\boldsymbol{n}}\hat{\boldsymbol{n}}$, is similar to our earlier work [6] but only acts near the substrate. This is accomplished through the addition of the term $G(\psi) = 18\psi^2(1-\psi)^2$, where ψ, for the bottom substrate, takes on the form

$$\psi_B(y) = \frac{1}{2} + \frac{1}{2}\tanh\{3[y_B + (\epsilon + \lambda/2) - y]/\lambda\}.$$

A similar expression is used for the top substrate. The inclusion of $G(\psi)$ results in active stresses confined to a band with width λ and located a distance ϵ away from the substrate (Fig. S1). Note that vertical height of the active stress is controlled by λ and that $\int G(\psi)dy = \lambda/2$.

Three examples of the velocity fields obtained numerically are shown in Fig. S4, corresponding to the cell motion on single substrate, confined in channels and confined in channels with asymmetric adhesion (Fig. 2 and Fig. 3 in main text). The retrograde flow patterns are similar to previous studies in[6].

NUMERICAL METHODS

The equation for ϕ is stepped by uniform time step $\Delta t = 2 \times 10^{-3}s$ in a forward Euler scheme so that ϕ at time step $n+1$ is obtained from ϕ at time step n:

$$\phi^{(n+1)} = \phi^{(n)} - \Delta t\boldsymbol{u} + \Delta t\Gamma[\epsilon\nabla^2\phi^{(n)} - G'(\phi^{(n)}) + \epsilon c^{(n)}|\nabla\phi^{(n)}|],$$

Here, $c^{(n)} = -\nabla\cdot(\nabla\phi^{(n)}/|\nabla\phi^{(n)}|)$ is computed using a finite difference method and all other differentiation operators are computed using a fast Fourier spectral method. Simulations were carried out on a 256×256 grid of size $50\mu m \times 50\mu m$. Model parameters, modified from [5, 6], are listed in Table S1.

The velocity field $\boldsymbol{u}$ is updated every time step by a semi-implicit Fourier spectral method after updating ϕ as detailed in [5]. The equation is iterated as:

$$\xi_0\boldsymbol{u}_{k+1} - \nu\tilde{\phi}\nabla^2\boldsymbol{u}_{k+1} = \nabla\cdot[\nu\phi\nabla\boldsymbol{u}_k + \nu(\phi - \tilde{\phi})\nabla\boldsymbol{u}_k^T] - \xi_s\chi\boldsymbol{u}_k + \boldsymbol{F},$$

where $\tilde{\phi} = 2$, and $\boldsymbol{F}$ represents the terms in the Stokes equation that are independent of the iteration step k. The iteration will continue until

$$\frac{\max|\boldsymbol{u}_{k+1} - \boldsymbol{u}_k|}{\max|\boldsymbol{u}_k|} < 0.1,$$

or until a maximal number of iterations (here chosen to be 20) is reached.

ANALYTICAL RESULTS

As stated in the main text, we aim to analytically solve Eq. S1&S2, where several simplifications have to be made. First, we are trying to find the steady-state solutions, so the cell shape will not change with time. Thus we drop Eq. S1 and, instead, put boundary conditions for Eq. S2. In accordance with our simulations, we choose slip boundary conditions, similar to[7]. The boundary condition for the steady-state cell shape is

$$\boldsymbol{u}\cdot\hat{\boldsymbol{n}} = \vec{v}_c\cdot\hat{\boldsymbol{n}},$$

where $\vec{v}_c$ is the cell's mass of center velocity, which is our target to solve, and $\hat{\boldsymbol{n}}$ is the normal unit vector of the boundary. The cell's boundary is free so the parallel stress at the boundary is zero

$$\hat{\boldsymbol{t}}\cdot\sigma^{vis} = 0,$$

where $\hat{\boldsymbol{t}}$ is the tangential unit vector of the boundary. Notice that the active stress is always constrained inside the cell so it will not enter any boundary conditions. The total force of the cell exerted on substrate should be balanced which gives a zero net traction force condition

$$\int \xi(\boldsymbol{r})\boldsymbol{u}d^2\boldsymbol{r} = 0,$$

where $\xi(\boldsymbol{r})$ is the friction coefficient at different locations. To get analytical expressions, we neglect the spatial heterogeneity in friction and simply take $\xi(\boldsymbol{r}) = \xi$. This simplification does not change the central feature of our main result (the cell's speed is inversely related to the cell's height).

Second, we only take into account the viscosity, friction and active stress because they are directly related to the cell motion. The adhesion, area conservation and membrane forces only contribute to the cell's shape, which is implicitly included in the boundary conditions. Thus we get a simplified equation for Eq. S2:

$$\nu\nabla\cdot\sigma^{vis} - \xi\boldsymbol{u} + \nabla\cdot\sigma^{a} = 0. \tag{S4}$$

Integrating the above equation and using the zero traction force condition, we obtain $\oint(\nu\sigma^{vis} + \sigma^{a})\cdot\hat{\boldsymbol{n}}dl = 0$. As the active stress σ^a is constrained inside the cell, this will lead to a condition equivalent to the zero traction force condition

$$\oint \hat{\boldsymbol{n}}\cdot\sigma^{vis}dl = 0,$$

which is the zero traction force condition we used below.

Notice that a fixed cell shape has to be given in order to apply the boundary conditions. Since we only care about the cell's mass of center velocity $\vec{v}_c$, and not the full solution for $\boldsymbol{u}$, we will next show how $\vec{v}_c$ can be obtained without knowing $\boldsymbol{u}$.

Analytical solution of the rectangular model cell

Here we wish to solve the Eq. S4 for a rectangular fixed cell shape $x \in [-L/2, L/2], y \in [0, H]$ with an unknown cell speed v_c (notice we put the x-direction as cell moving direction so v_c is a scalar). The boundary conditions are $\boldsymbol{u}_x(x = \pm L/2) = v_c,\ \boldsymbol{u}_y(y = 0, H) = 0,$ and $\int \boldsymbol{u}\mathrm{dxdy} = 0$. Integrating the Stokes equation, we get $\int d^2\boldsymbol{r}(\nu\nabla\cdot\sigma^{vis} + \nabla\cdot\sigma^{a}) = \oint(\nu\sigma^{vis}\cdot\boldsymbol{n} + \sigma^{a}\cdot\boldsymbol{n})dl = \xi\int \boldsymbol{u}d^2\boldsymbol{r} = 0$. Note that the active stress σ^a should be constrained within the cell [7] resulting in the zero net traction force condition $\oint \sigma^{vis}\cdot\boldsymbol{n}dl = 0$. This means $\int[\sigma^{vis}_{xx}(x = L/2) - \sigma^{vis}_{xx}(x = -L/2)]dy = \int[\partial_x\boldsymbol{u}_x|_{x=L/2} - \partial_x\boldsymbol{u}_x|_{x=-L/2}]dy = 0$ and $\int[\sigma^{vis}_{xy}(y = H) - \sigma^{vis}_{xy}(y = 0)]dx = 0$ due to the rectangular shape.

The tangential vector $\hat{\boldsymbol{t}}$ can be determined by the normal vector $\hat{\boldsymbol{t}}_x = -\hat{\boldsymbol{n}}_y, \hat{\boldsymbol{t}}_y = \hat{\boldsymbol{n}}_x$. The zero-parallel stress condition $\hat{\boldsymbol{t}}\cdot\sigma^{vis} = 0$ results in

$$\hat{\boldsymbol{n}}_y\sigma^{vis}_{xx} - \hat{\boldsymbol{n}}_x\sigma^{vis}_{xy} = 0,\ \ \hat{\boldsymbol{n}}_y\sigma^{vis}_{xy} - \hat{\boldsymbol{n}}_x\sigma^{vis}_{yy} = 0.$$

For rectangular boundaries, these conditions lead to

$$\sigma^{vis}_{xy} = 0, \tag{S5}$$

at all boundaries.

Since the cell is moving along x-direction, only $\boldsymbol{u}_x$ is relevant and we can integrate the 2D Stokes equation in the y-direction. With the condition of $\sigma^{vis}_{xy} = 0$, we obtain a 1D Stokes equation:

$$2\nu\frac{\partial^2\tilde{\boldsymbol{u}}_x}{\partial x^2} - \xi\tilde{\boldsymbol{u}}_x + \frac{\partial\tilde{\sigma}^a_{xx}}{\partial x} = 0, \tag{S6}$$

where $\tilde{\boldsymbol{u}}_x = \int_0^H \boldsymbol{u}_x dy$, and $\tilde{\sigma}^a_{xx} = \int_0^H \sigma^a_{xx}dy$. The corresponding boundary conditions are $\tilde{\boldsymbol{u}}_x(L/2) = \tilde{\boldsymbol{u}}_x(-L/2) = v_cH$ and $\partial_x\tilde{\boldsymbol{u}}_x|_{x=L/2} = \partial_x\tilde{\boldsymbol{u}}_x|_{x=-L/2}$. This is exactly the same problem as in reference [7]. Using standard Green's function methods, we obtain:

$$\tilde{\boldsymbol{u}}_x(L/2) = -\frac{1}{4\nu}\int_{-L/2}^{L/2}\frac{\tilde{\sigma}^a_{xx}\sinh(\kappa x)}{\sinh(\kappa L/2)}dx,$$

and, since $\boldsymbol{u}_x = v_c$ at boundaries $x = \pm L/2$, we obtain

$$v_c = \frac{\tilde{\boldsymbol{u}}_x(L/2)}{H}, \tag{S7}$$

as reported in the main text (Eq. 5). If the active stress is confined in a band with width λ, i.e., $\int_0^H \sigma^a_{xx} dy = \lambda f(x)$, the cell's speed v_c will scale as:

$$v_c = \frac{\lambda v_0}{H}, \tag{S8}$$

where v_0 is a constant, corresponding to the boundary velocity determined by the 1D problem $2\nu\partial_x^2 v - \xi v + f'(x) = 0$ with homogeneous boundary conditions. Notice that this scaling does not depend on the vertical position of the active stress. Therefore, our model will give the same cell speed independent of the type of active stress (actin polymerization, myosin contraction), as long as the integrated active stress is the same.

Effective height for non-rectangular cells

In the above section, the speed of a rectangular cell was determined exactly. Actual cells are, of course, not rectangular but obtaining a solution for cells with more complex shapes is challenging. Nevertheless, insight can be obtained by considering a cell composed of two rectangles, one positioned at $[-L, 0] \times [0, H_2]$ and one positioned at $(0, L] \times [0, H_1]$ ($H_1 < H_2$ (see Fig. S5). We take the active stress to be located at the latter (right) rectangle. This problem has the same boundary conditions as above, with two additional continuity conditions:

$$\boldsymbol{u}_x(x = 0^+) = \boldsymbol{u}_x(x = 0^-), \quad \partial_x \boldsymbol{u}_x|_{x=0^+} = \partial_x \boldsymbol{u}_x|_{x=0^-}. \tag{S9}$$

To simplify the problem, we introduce the new variables $u_1 = \int_0^{H_1} \boldsymbol{u}_x dy$ and $u_2 = \int_0^{H_2} \boldsymbol{u}_x dy$. Using the continuity condition we have:

$$u_2(0^-) = \int_0^{H_2} \boldsymbol{u}_x(x = 0^-) dy = \int_{H_1}^{H_2} \boldsymbol{u}_x(x = 0^-) dy + \int_0^{H_1} \boldsymbol{u}_x(x = 0^+) dy = (H_2 - H_1) v_c + u_1(0^+).$$

Together with $u_1(L) = H_1 v_c$, $u_2(-L) = H_2 v_c$ we get

$$u_2|_{-L}^0 + u_1|_0^L = 0. \tag{S10}$$

The zero traction force will give

$$\int_0^{H_2} \partial_x \boldsymbol{u}_x|_{x=-L} dy = \int_{H_1}^{H_2} \partial_x \boldsymbol{u}_x|_{x=0} dy + \int_0^{H_1} \partial_x \boldsymbol{u}_x|_{x=L} dy.$$

Combining with the stress continuity we obtain

$$\partial_x u_2|_0 = \int_0^{H_2} \partial_x \boldsymbol{u}_x|_{x=0} dy = (\int_0^{H_1} dy + \int_{H_1}^{H_2} dy)(\partial_x \boldsymbol{u}_x|_{x=0}) = \partial_x u_1|_0 + \partial_x u_2|_{-L} - \partial_x u_1|_L.$$

such that

$$\partial_x u_2|_{-L}^0 + \partial_x u_1|_0^L = 0. \tag{S11}$$

Notice that Eq. S10 and Eq. S11 have clear physical meanings, namely flow conservation and force balance, respectively. It is convenient to introduce the net flow C and net force F on each rectangle:

$$u_2|_{-L}^0 = C, \;\; u_1|_0^L = -C, \;\; \partial_x u_2|_{-L}^0 = F, \;\; \partial_x u_1|_0^L = -F,$$

and, using the zero-parallel stress condition, we obtain the 1D version of the problem for the right and left rectangle:

$$2\nu\partial_x^2 u_2 - \xi u_2 = 0, \quad 2\nu\partial_x^2 u_1 - \xi u_1 + \partial_x \sigma^a = 0,$$

with $\sigma^a = \int_0^{H_1} \sigma_{xx} dy$. u_1 can be solved by superposition of two parts: $\tilde{u}_1$ with homogeneous boundary conditions and active stress, and $\hat{u}_1$ with inhomogeneous boundary conditions but zero active stress. After substituting $u_1 = \tilde{u}_1 + \hat{u}_1$, we obtain

$$2\nu\partial_x^2 \tilde{u}_1 - \xi \tilde{u}_1 + \partial_x \sigma^a = 0, \; \tilde{u}_1|_0^L = 0, \; \partial_x \tilde{u}_1|_0^L = 0,$$

and

$$2\nu\partial_x^2\hat{u}_1 - \xi\hat{u}_1 = 0,\ \hat{u}_1|_0^L = -C,\ \partial_x\hat{u}_1|_0^L = -F.$$

We can then solve for $\tilde{u}_1, \hat{u}_1$ and u_2 and obtain the boundary velocity:

$$H_1 v_c = u_1(L) = v_a - \frac{C}{2} - \frac{\alpha F}{2\kappa},\ \ H_2 v_c = u_2(-L) = -\frac{C}{2} + \frac{\alpha F}{2\kappa}, \tag{S12}$$

and the boundary stresses:

$$\partial_x u_2|_{-L} = -\frac{F}{2} + \frac{\alpha\kappa C}{2}, \partial_x u_2|_0 = \frac{F}{2} + \frac{\alpha\kappa C}{2}, \partial_x u_1|_0 = \pi_a + \frac{F}{2} - \frac{\alpha\kappa C}{2}, \partial_x u_1|_L = \pi_a - \frac{F}{2} - \frac{\alpha\kappa C}{2}, \tag{S13}$$

where $\kappa = \sqrt{\xi/2\nu}, \alpha = \coth(\kappa L/2)$. v_a and π_a are the boundary speed and boundary stress from the homogeneous equation of $\tilde{u}_1$, which are constants.

To calculate v_c, we have to determine C and F. Eq. S12 gives one condition $H_1/H_2 = u_1(L)/u_2(L)$ and an additional condition from the stresses in Eq. S13 is needed. Unfortunately, there is no simple relation between the four equalities in Eq. S13 since the stress continuity equation cannot be defined at the boundary at $x = 0$ and between $y = H_1$ and $y = H_2$. Instead, we assume that the ratio of the integrated stress at $x = 0$ satisfies $(\partial_x u_1|_0)/(\partial_x u_2|_0) = \beta$. Then, we have:

$$v_c = \frac{\kappa v_a \alpha^2(1+\beta) + \kappa v_a(1-\beta) - 2\alpha\pi_a}{\kappa[\alpha^2(1+\beta)(H_1+H_2) + (\beta-1)(H_1-H_2)]}. \tag{S14}$$

Note that when $H_1 = H_2$, corresponding to $\beta = 1$, this result gives the same scaling as for the simple rectangular shape.

With $\alpha \gg 1$, corresponding to a highly viscous cytoskeleton, we have

$$v_c \approx \frac{v_a}{H_1 + H_2} - \frac{2\pi_a}{\kappa\alpha(1+\beta)(H_1+H_2)}, \tag{S15}$$

which clearly shows that the cell speed is scaling inversely with the average height $(H_1 + H_2)/2$.

TEST OF MODEL PREDICTIONS

The above analysis indicates that the ratio of the height of stress band λ and the cell height H determines the cell speed. Thus, cells with equal ratio should have similar speeds. To test this explicitly, we simulated cells in chambers with heights varying between $h = 4\mu m$ and $h = 10\mu m$, constraining the cell's height, while keeping the ratio $\lambda/h = 0.5$. Cells shapes for three different chamber heights are shown in Fig. S7a while the cell speed and effective height as a function of chamber height are shown in Fig. S7b and c, respectively. Clearly, the results from Fig. S7b show that the speed of the cell is independent of the chamber height, consistent with our model prediction.

In addition, our derived expression predicts that if $\lambda = H$, corresponding to an active stress region that spans the entire height of the cell, the cell speed should be independent of the chamber height. To verify this, we performed simulations of confined cells with the active stress at the entire cell front. To this end, we no longer constrain the stress to a narrow band and, instead, use $\sigma^a = -\phi\rho_a(1-\chi)\epsilon|\nabla\phi|^2\hat{\boldsymbol{n}}\hat{\boldsymbol{n}}$. We introduce the factor of $1-\chi$ to prevent protrusion in the region where the cell and substrate overlap, something that is excluded from occurring in other models when the band restricts protrusion. Resulting cell shapes for different chamber heights are shown in Fig. S8a. In Fig. S8b, we plot the cell speed as a function of the chamber height and in the Fig. S8 we plot the effective height. As expected, the cell speed changes little as the chamber height is varied, again consistent with our predictions.

OSCILLATORY PROTRUSIONS

Results in the main text are for cells with constant active stress, resulting in constant cell shapes. Such constant shapes are applicable to fish keratocytes, fast moving cells that maintain their morphology [8]. Other cell types, however, including neutrophils and *Dictyostelium discoideum* cells [9], move in a more time-dependent way, with repetitive and short-lived protrusions called pseudopods. To determine the dependence of cell speed on chamber height for these

types of cells we introduce an oscillatory modulation to the active stress: $\sigma^a = -\phi\rho_a G(\psi)\sin(2\pi t/T)\epsilon|\nabla\phi|^2\hat{\boldsymbol{n}}\hat{\boldsymbol{n}}$. Here, T is the period of the oscillation cycle which can be varied. Results from additional simulations show that the cell speed gets larger as the substrate adhesion is increased (Fig. S12a). This dependence on adhesion was found to be largely independent of the period and is similar to the one found for model cells with constant stress (Fig. 2b). Also consistent with our results in the main text (Fig. 2c), the effective height is again inversely related to the adhesion strength.

EXPERIMENTS

Cell culture and preparation

Wild type Dictyostelium discoideum (AX4) cells were transformed with a construct in which the regulatory region of actin 15 drives genes encoding a fusion of GFP to LimE (Δ coil LimE-GFP) and a gene encoding a fusion of RFP to Coronin (LimE GFP/corA RFP)[10]. Cells were transformed with the plasmid pDM115 cAR1-RFP (Hygromycin resistance) to visualize the membrane. Cells were grown in a shaker, containing 35.5g HL5 media (®FORMEDIUM)/L of DI water[11] in a shaker. When cells reached their exponential phase ($1-2\times10^6$ cells/mL), they were harvested by centrifugation, washed in KN_2/Ca buffer (14.6 mM KH_2PO_4, 5.4 mM Na_2HPO_4, 100 μM $CaCl_2$, pH 6.4), and resuspended in KN_2/Ca at 10^7 cells/mL. The washed cells were developed for 5h with pulses of 50 nM cAMP added every 6 min.

Microfluidic device

The design of microfluidic device used in the study is similar to the design of the devices that were previously used to study gradient sensing in yeast[12] and chemotaxis in Dictyostelium[13, 14]. The microfluidic device (Fig. S9) consists of a lithographically fabricated silicone (polydimethylsiloxane, PDMS, Sylgard 184) chip and a cover glass substrate (with either PDMS or hydrogel coating, see below), against which the chip is sealed using vacuum suction. To this end, the network of liquid-filled microfabricated microchannels of the chip, which are relatively narrow and either 100 or 10 μm deep, is surrounded by a wide ($\sim$6 mm) and deep ($\sim$1 mm) groove, serving as a vacuum cup. When the PDMS chip is placed on a substrate, the application of vacuum to the cup generates a pulling force that instantly seals the liquid-filled microchannels of the chip against the substrate. The application of vacuum also leads to controlled partial collapse of the microchannels, making it possible to reduce the depth of the 10 μm deep microchannels by $> 5\mu$m by controlling the level of vacuum. The network of liquid-filled microchannels of the device (Fig. S9) has a single outlet (out), two main inlets, for a C_0 =100nM solution of cAMP (in 1) and for buffer (in 2), and an auxiliary inlet for cell loading (in c). The functional region of the device has two mirror-symmetric 100 μm deep, 500 μm wide flow-through channels (Fig. S9), which are connected to the two main inlets and are flanking 3 clusters of 10 μm deep gradient chambers. The flow through the device is driven by applying equal differential pressures of $\sim$2 kPa between the two main inlets and the outlet. The resulting mean flow velocity in the 500 μm wide flow-through channels is $\sim$200 μm/s. The gradient chambers are all 70 μm wide and each cluster has 15 identical chambers with equal lengths. The lengths L of the gradient chambers in the upstream, middle, and downstream clusters are 360, 220, or 120 μm, respectively. There is practically no flow through the gradient chamber because of near zero pressure gradient along them, and the diffusion of cAMP from the flow-through channel perfused with the 100 nM solution to the flow-through channel perfused with buffer results in linear concentration profiles of cAMP with gradients of 0.28, 0.45, and 0.83 nM/μm, respectively. In different sets of experiments, the application of different levels of vacuum resulted in the effective depths of the gradient chambers of 10, 7, and 5 μm.

Substrate preparation

In our experiments, the microfluidic chips were sealed against cover glass substrates with two different types of coating: $\sim$10 μm thick layer of PDMS of the same type as the material of the chip and $\sim$3 μm thick layer of 30% polyethylene glycol (PEG) gel. In the former case, the cover glass was a #1.5 thickness 47 mm circle at the bottom of a 50 mm WillCo cell culture dish. A small amount ($\sim$0.2 mL) of PDMS pre-polymer (10:1 mixture of base and curing agent of Sylgard 184 by Dow Corning) was dispensed onto the cover glass. Spin-coating was made at 6000 rpm for 2 min, and PDMS was cured by overnight baking in a 60°C oven. In the latter case, the cover glass was #2,

50x35 mm rectangle. The cover glass was cleaned with water and ethanol, dried, air-plasma treated for 10 s, and then exposed to 3-(Trimethoxysilyl) propyl Methacrylate (®Aldrich) vapor at 75°C for 30 min. A 30% PEG pre-polymer solution was prepared by mixing PEG diacrylate (PEG-DA; avg Mn 900, ®Aldrich) with a 0.03% aqueous solution VA086 (300 μg dissolved in 1000 μL of DI water) in a 3:7 ratio by volume. VA086 is iLine (365nm) sensitive UV photo-initiator that cross-links PEG-DA molecules (thus, converting a PEG-DA solution into a PEG gel) by binding to the acrylate groups and also links PEG-DA chains to the acrylate groups on the glass surface. An $\sim$100μL drop of the solution was dispensed onto the center of the cover glass and squeezed to a thin layer by placing an untreated #1.5 thickness, 30 mm diameter round cover glass on top, gently pushing this second cover glass with a pipette tip, and removing the excess solution with a wipe. The cross-linking of PEG-DA was done by exposing it to a total of 2.19 J/cm^2 of 365 nm UV (derived from 365nm UV LEDs; $\sim$365 mW/cm^2 for 60 sec). After the round cover glass was removed, the 50x35 mm cover glass had an $\sim$4 μm thick layer of covalently bonded PEG gel in the middle.

Data acquisition and image analysis

Differential interference contrast (DIC) images were taken of all gradient chambers on a spinning-disk confocal Zeiss Axio Observer inverted microscope using a 10x objective and a Roper Cascade QuantEM 512SC camera. DIC images were captured every 15 s for 30 min and were used to calculate the speed of the cells. To obtain the shape of the cells, fluorescent images (488 nm and 561 nm excitation) were captured every 2 seconds with a 63X oil objective. To visualize the shape of the cells near the substrates, z-stacks of confocal images were collected.

The centroids of all cells were tracked across the gradient chambers from 10X image sequences using Slidebook 6 (Intelligent Imaging Innovations) software. Cells that moved more than 5 frames without encountering another cell were chosen for data analysis. 50 to 100 cell tracks were analyzed in each experiment. Velocity in the gradient direction, $V_x(t)$, was computed using data from frames 45 s apart with Matlab R2016a (The MathWorks, Natick, MA). We have verified that cell speeds were largely independent of their positions within the gradient chambers. Consequently, the average speed was defined as the mean speed of all cells at least 30μm from the sides of the chamber adjacent to the flow-through channels at all recorded times.

Cells outlines near the top (PDMS chip) and the bottom (substrate, PDMS or PEG) of the gradient chambers were obtained from confocal fluorescence images at 63X magnification with a custom-made Matlab code, as follows. After removing the average background intensity value, images were binarized using a threshold that was dependent on the cell's maximum intensity. Matlab algorithms were then used to dilate images, to fill possible holes, to erode images, to smooth images, and to provide information (area and outlines) about the connected pixels of the binary image. Finally, using the resulting images, we computed the ratio between the cell contact area at the top and bottom of the chamber and averaged this ratio over three time points for each cell.

Statistics and reproducibility

Each experiment was carried out four or five times on different days and the data were averaged for N=200-300 cells. Cell speed was found to be approximately normally distributed and p-values were computed with the unpaired t-test. For the area size ratio, the data distribution was not normal, and the Wilcoxon rank-sum test was used to obtain the p-values. The variations of the cell speed with the gradient chamber height and the type of substrate coating (PDMS vs. PEG) followed the same trends in gradient chambers of different lengths, L (cf. Fig. 4d and Fig. S11).

[1] B. A. Camley, Y. Zhang, Y. Zhao, B. Li, E. Ben-Jacob, H. Levine, and W.-J. Rappel, Proc Natl Acad Sci U S A **111**, 14770 (2014).
[2] Y. Zhao, Y. Ma, H. Sun, B. Li, and Q. Du, arXiv preprint arXiv:1712.01951 (2017).
[3] K. A. Brakke, Experimental mathematics **1**, 141 (1992).
[4] D. Shao, W.-J. Rappel, and H. Levine, Physical Review Letters **105**, 108104 (2010).
[5] B. A. Camley, Y. Zhao, B. Li, H. Levine, and W.-J. Rappel, Physical Review Letters **111**, 158102 (2013).
[6] D. Shao, H. Levine, and W.-J. Rappel, Proc Natl Acad Sci U S A **109**, 6851 (2012).
[7] A. Carlsson, New journal of physics **13**, 073009 (2011).
[8] K. Keren, Z. Pincus, G. M. Allen, E. L. Barnhart, G. Marriott, A. Mogilner, and J. A. Theriot, Nature **453**, 475 (2008).

[9] H. Levine and W.-J. Rappel, Phys Today **66** (2013), 10.1063/PT.3.1884.
[10] D. Fuller, W. Chen, M. Adler, A. Groisman, H. Levine, W.-J. Rappel, and W. F. Loomis, Proc Natl Acad Sci U S A **107**, 9656 (2010).
[11] M. Sussman, in *Methods in cell biology*, Vol. 28 (Elsevier, 1987) pp. 9–29.
[12] S. Paliwal, P. A. Iglesias, K. Campbell, Z. Hilioti, A. Groisman, and A. Levchenko, Nature **446**, 46 (2007).
[13] M. Skoge, M. Adler, A. Groisman, H. Levine, W. F. Loomis, and W.-J. Rappel, Integrative Biology **2**, 659 (2010).
[14] M. Skoge, H. Yue, M. Erickstad, A. Bae, H. Levine, A. Groisman, W. F. Loomis, and W.-J. Rappel, Proc Natl Acad Sci U S A **111**, 14448 (2014).

Parameter	Description	Value
γ	Tension	20 pN
ϵ	Width of phase field	2 μm
A_0	Cell area size	120 μm^2
M_a	Cell area conservation strength	20 pN/μm
Γ	Phase field relaxation parameter	0.4 $\mu m/s$
ν	Cell viscosity	10^2 pN s/μm
ξ_d	Damping coefficient	0.05 Pa s/μm
ξ_s	Substrate friction coefficient	5 Pa s/μm
η_a	Active protrusion coefficient	10^3 pN μm^2
λ	Width of active stress confinement	2 μm
δ	Width of the substrate phase field	1 μm
g	Substrate repellent coefficient	5×10^3 pN/μm

TABLE S1: Model Parameters

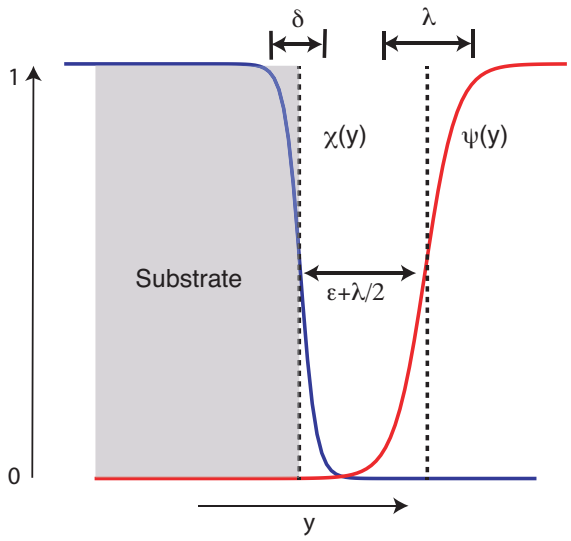

FIG. S1: Illustration of the substrate field χ, with width δ, together with the protrusion band ψ, with width λ and located a distance of ϵ away from the substrate.

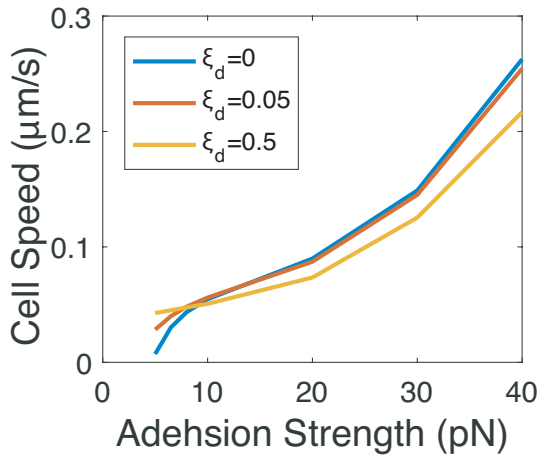

FIG. S2: Cell speed as a function of adhesion strength for different values of the drag coefficient ξ_d (in units of Pa s/μm). Cell speed changes little as ξ_d is increased from 0 to 0.5.

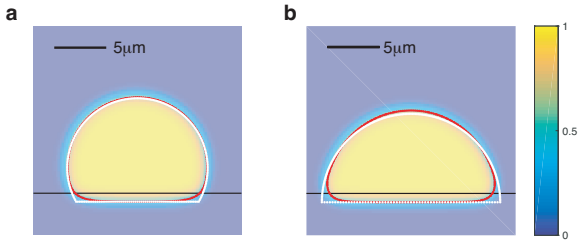

FIG. S3: Simulation results of the phase-field method without active force (red line) compared to results obtained using Surface Evolver (white dots). The phase field is plotted using the indicated color scale. (a). Adhesion strength 10 pN. (b). Adhesion strength 20 pN.

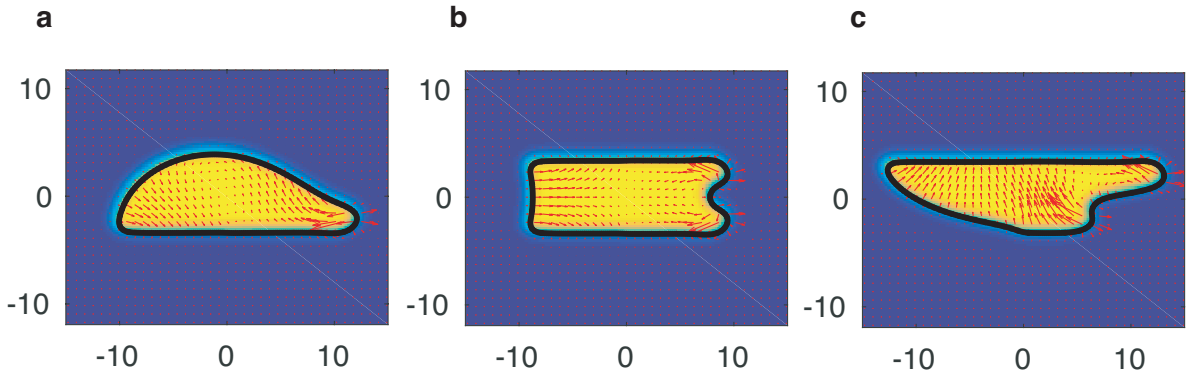

FIG. S4: Numerical results showing the phase field using a color scale, the outline of the cell in black (defined as $\phi = 1/2$), and the actin fluid velocity (multiplied with the phase field ϕ) for a cell moving on a single substrate (a), and confined in a channel with equal (b) and unequal substrate adhesion (c). Arrows indicate the direction of the velocity and the arrow length indicates the amplitude of the velocity.

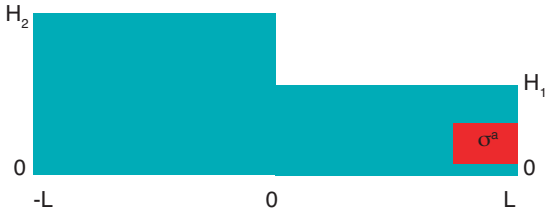

FIG. S5: Schematic illustration of the non-deformable cell considered here, consisting of two rectangles of unequal height. Active stress occurs in the right (front) rectangle.

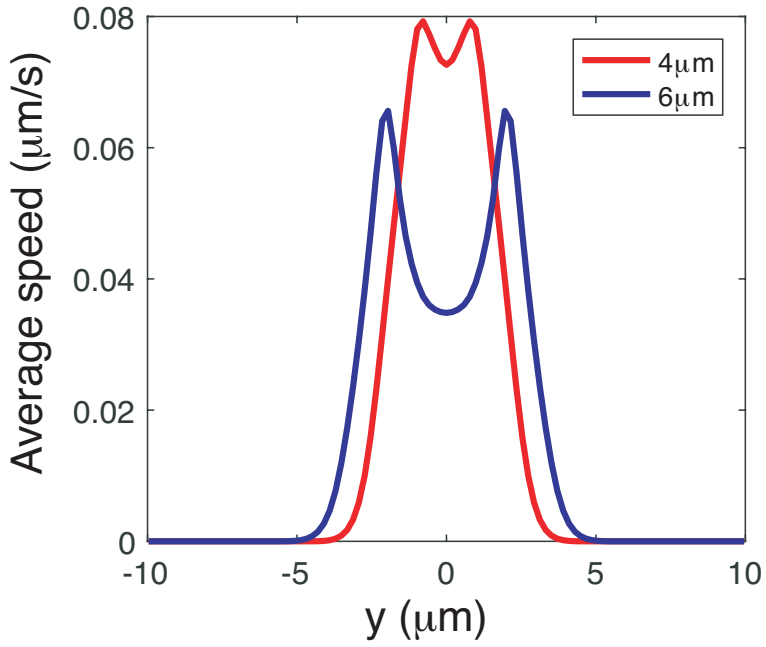

FIG. S6: The average speed along the y-direction, defined as $1/L \int |\phi u_x| dx$, for a cell in a confined chamber with a height of $h = 4\mu$m (red line) and $h = 6\mu$m (blue line). The vertical shear dissipation increases with increasing cell height.

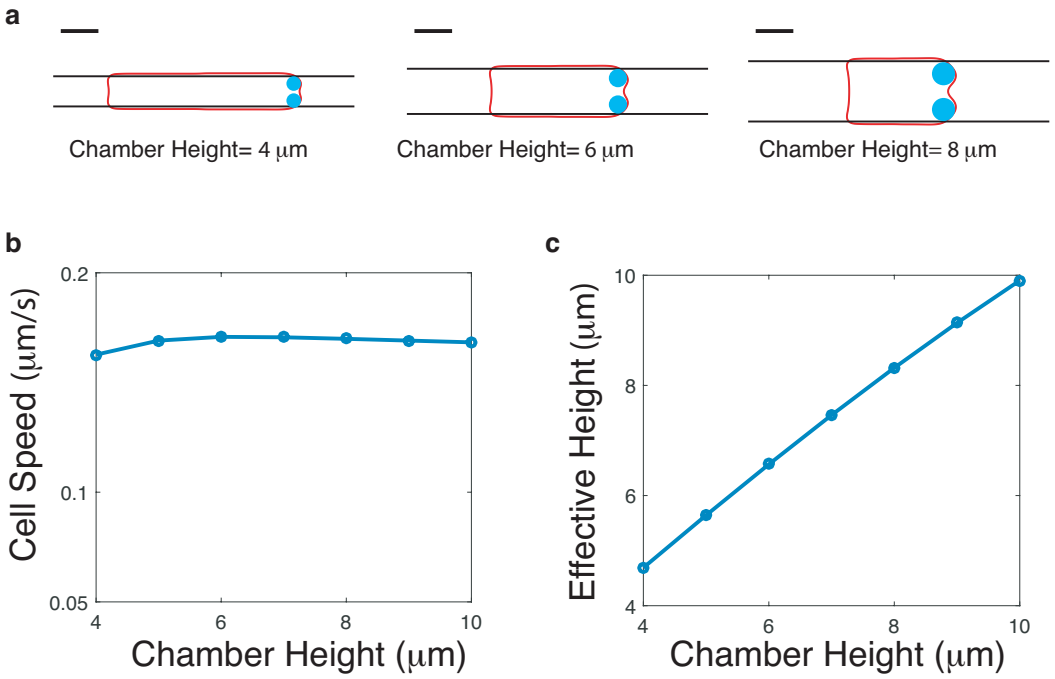

FIG. S7: Simulation results of cells with a constant ratio 0.5 of the width of active stress band and the chamber height. The cyan dots schematically indicate the active stress sites. (a) Cell shapes for different chamber heights. Scalebar=5 μm (b) Cell speed as a function of chamber height. (c) Effective height as a function of chamber height.

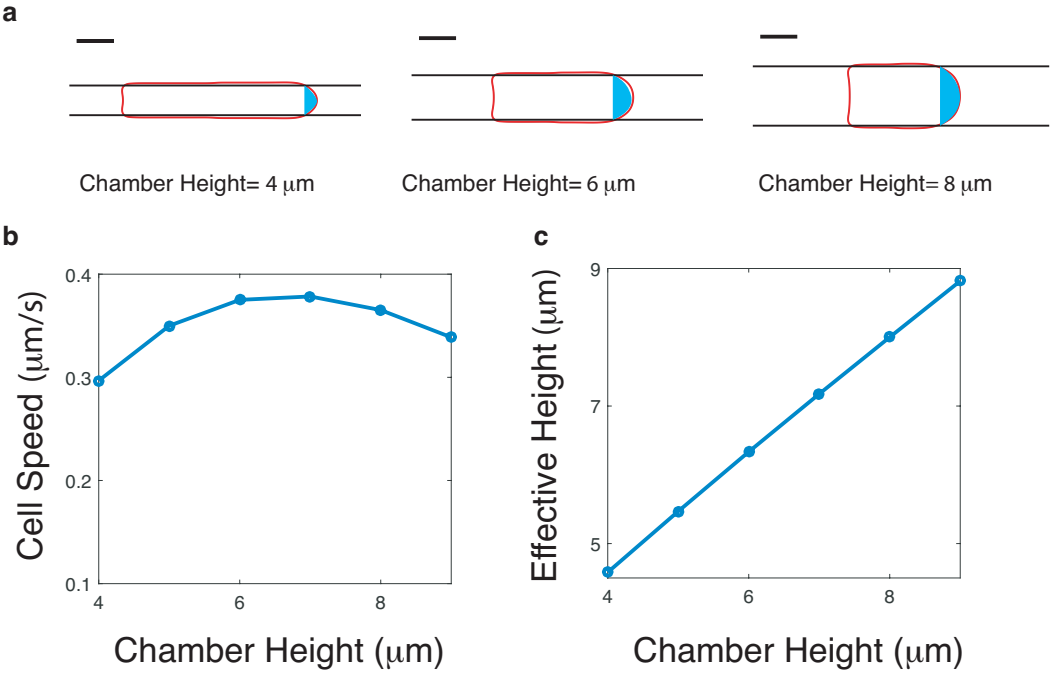

FIG. S8: Simulation results of cells with active stress at the entire front, as indicated. (a) Cell shapes for different chamber heights. Scalebar=5μm (b) Cell speed as a function of chamber height. (c) Effective height as a function of chamber height.

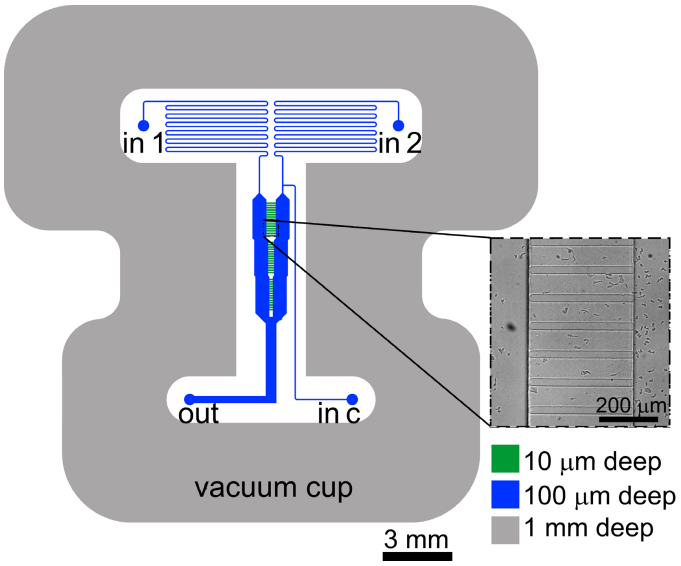

FIG. S9: Design of the microfluidic device. The enlarged image is the experimental DIC view using a 10x objective showing gradient chambers and flow chambers with cells.

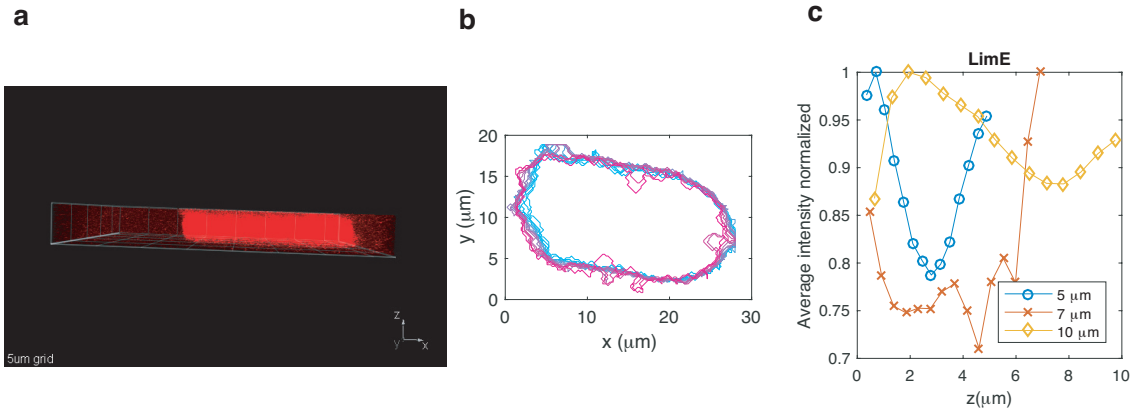

FIG. S10: Experimentally obtained cell shapes and F-actin distribution for a cell moving in a 5 μm high channel. (a) z-stack of a cell containing the fluorescent membrane marker Car1-RFP. The cell extends from top to bottom PDMS substrate. (b) Cell outlines for different z values ranging from 0 (magenta) to 5 μm (cyan). The outline is essentially identical for all z values. (c) Average fluorescence intensity (normalized) of LimE, an F-actin marker, for each confocal slice as a function of z for representative cells in channels with height of 5,7 and 10 μm. All cells examined (N=5) displayed a qualitatively similar pattern with increased intensity close to the substrates.

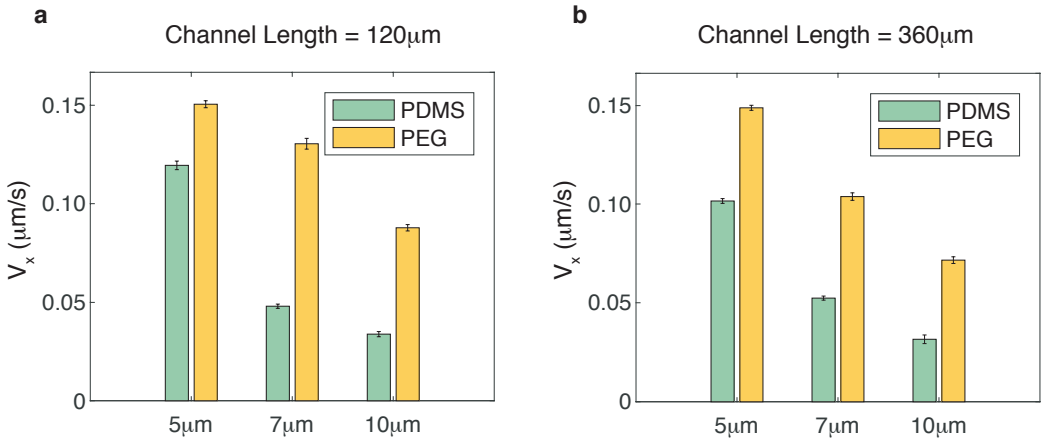

FIG. S11: Average cell speed for different chamber heights and substrate composition for channel length $L = 120\mu$m, corresponding to a gradient of 0.83 nM/μm, and $L = 360\mu$m, corresponding to a gradient of 0.28 nM/μm.

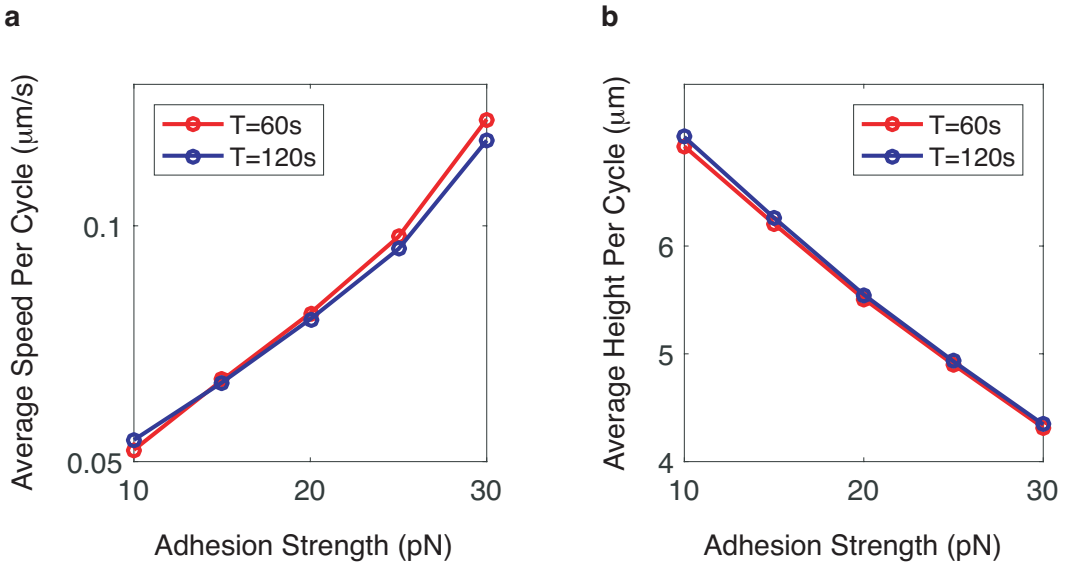

FIG. S12: Cell speed and effective height for cells with oscillatory active stress. (a) Average cell speed, computed as moving distance divided by cycle time, and (b) effective height as a function of substrate adhesion strength. Shown are the results for oscillatory stress cycles with two different periods.